

Annual Review of Biophysics

Hydrogel-Tissue Chemistry: Principles and Applications

Viviana Gradinaru,¹ Jennifer Treweek,¹
Kristin Overton,² and Karl Deisseroth^{2,3,4}

¹Division of Biology and Biological Engineering, California Institute of Technology, Pasadena, California 91125, USA; email: viviana@caltech.edu

²Department of Bioengineering, Stanford University, Stanford, California 94305, USA; email: deissero@stanford.edu

³Department of Psychiatry and Behavioral Sciences, Stanford University, Stanford, California 94305, USA

⁴Howard Hughes Medical Institute, Stanford University, Stanford, California 94305, USA

Annu. Rev. Biophys. 2018. 47:355–76

The *Annual Review of Biophysics* is online at
biophys.annualreviews.org

<https://doi.org/10.1146/annurev-biophys-070317-032905>

Copyright © 2018 by Annual Reviews.
All rights reserved

Keywords

CLARITY, hydrogels, metareactant, HTC, hydrogel-tissue, clearing

Abstract

Over the past five years, a rapidly developing experimental approach has enabled high-resolution and high-content information retrieval from intact multicellular animal (metazoan) systems. New chemical and physical forms are created in the hydrogel-tissue chemistry process, and the retention and retrieval of crucial phenotypic information regarding constituent cells and molecules (and their joint interrelationships) are thereby enabled. For example, rich data sets defining both single-cell-resolution gene expression and single-cell-resolution activity during behavior can now be collected while still preserving information on three-dimensional positioning and/or brain-wide wiring of those very same neurons—even within vertebrate brains. This new approach and its variants, as applied to neuroscience, are beginning to illuminate the fundamental cellular and chemical representations of sensation, cognition, and action. More generally, reimagining metazoans as metareactants—or positionally defined three-dimensional graphs of constituent chemicals made available for ongoing functionalization, transformation, and readout—is stimulating innovation across biology and medicine.



ANNUAL
REVIEWS **Further**

Click here to view this article's
online features:

- Download figures as PPT slides
- Navigate linked references
- Download citations
- Explore related articles
- Search keywords

Contents

INTRODUCTION	356
DEVELOPMENT OF METHODS	357
HYDROGEL-TISSUE CHEMISTRY-BASED DISCOVERY IN NEUROSCIENCE AND THROUGHOUT THE ORGANISM	365
NONNEURAL TISSUES	366
OUTLOOK	368

INTRODUCTION

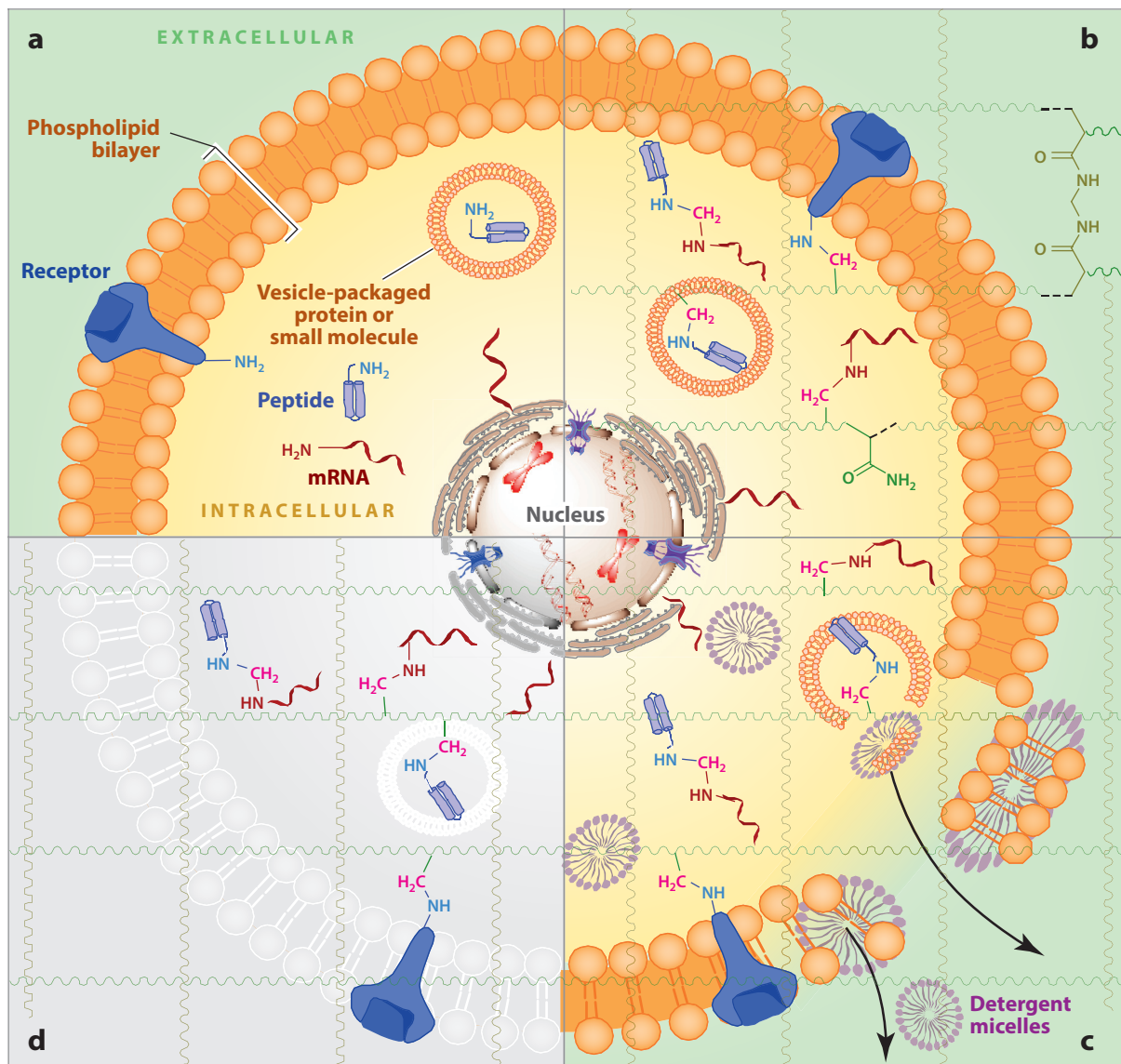
In the study of complex biological systems, a powerful experimental approach is that of analysis or disassembly (removing components, such as a particular type of cell or complex of molecules, from the native context for further study). For example, the current revolution in cancer treatment was in part enabled by reductionist molecular and cellular-level analysis of isolated cancer cells and of specific immune-system cells that play a role in suppressing tumor growth. The success of this analytical paradigm has, in part, extended to neuroscience as well; studies of isolated neurons and axons have facilitated elucidation of the fundamental logic of single-neuron information processing.

However, for systems like the intact vertebrate brain (composed of 10^7 – 10^{11} interconnected neurons and characterized by crucial emergent properties), studying constituent components in isolation can provide little insight into many of the most significant mysteries. Alternatively, converting the brain—or more broadly the entire metazoan (multicellular animal) organism—into an assembly of reactants anchored onto a new and versatile three-dimensional (3D) coordinate system has recently emerged as a complementary strategy (23, 24). Coupling individual subsets of chemically defined biomolecules to functional groups, covalently anchoring or entangling these in turn within a polymer lattice, and then working with this structure (effectively a 3D assembly of spatially tagged molecular reactants) (23, 24) has already opened the door to a diverse array of novel approaches and discoveries in biology.

The technique builds in part from (among several other foundations in science and engineering) the chemistry of hydrogels, which are 3D polymeric networks of connected hydrophilic components. Gels and polymers have a long history of use in biology, including for providing physical support of tissues during sectioning and imaging, as well as for a number of important clinical applications in regenerative medicine and tissue engineering. But in the basic science of hydrogel-tissue chemistry (23, 24), specific classes of native biomolecules in tissue are immobilized or covalently anchored (for example, through individualized interface molecules to gel monomer molecules) and precisely timed polymerization causing tissue-gel hybrid formation is triggered within all the cells across the tissue in an ordered and controlled process (**Figure 1**) to ultimately create an optically and chemically accessible biomolecular matrix. Indeed, when the biomolecules of interest are thereby transferred to the polymer lattice, a robust new composite hydrogel-tissue material results (23, 24), which becomes the substrate for future chemical and optical interrogation that can be probed and manipulated in new ways. This approach has been diversified (**Figure 2**) to address needs and opportunities in organisms and tissues across biology (including in cancer diagnostics, bacterial and HIV infection of mammalian tissues, developmental biology, parkinsonism, Alzheimer's disease, multiple sclerosis, autism, drug abuse, and fear/anxiety disorders). Here, we review the fundamentals of this approach, the rapidly expanding scope of discoveries that have resulted, and emerging directions and opportunities for the future.

DEVELOPMENT OF METHODS

Biomolecule functionalization and multistep linkage to a versatile tissue-hydrogel scaffold (**Figure 2**) within the cells of vertebrates (mouse, fish, and human) (15, 16, 23) were described in an initial version called CLARITY; this method was optimized for application to the vertebrate nervous system (15, 16, 23). The hydrogel-tissue hybrid brains were transparent (i.e., clarified) and had



NH_2 Amino group of nucleophilic small-molecule, peptide N-terminus, or amino acid side chain, e.g., lysine's ϵ -amine

CH_2 Carbonyl carbon of cross-linking fixative, e.g., formaldehyde

NH_2 Amino group or pyrimidine ring nitrogen of nucleic acids, e.g., adenosine, guanosine

NH_2 Amide group of biomolecule-trapping gel monomer, e.g., acrylamide

(Caption appears on following page)

Figure 1 (Figure appears on preceding page)

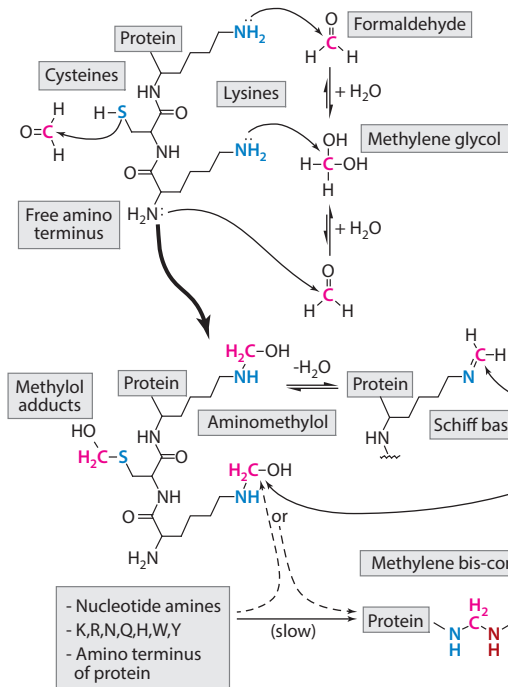
Hydrogel-tissue chemistry (HTC) steps toward tissue functionalization. The example shown (initial HTC formulation) is termed CLARITY (16). The main steps for transformation of the tissue, as shown for (a) the diagrammed cell prior to the HTC process, include (b) hydrogel-monomer infusion followed by cross-linking to native macromolecules and then gelation (*dashed black lines* denote newly formed C-C bonds to the hydrogel lattice, which in turn is shown as *wavy green lines*). Details of the chemistry are shown in **Figure 2**. For all figures, the color code for tracking source of C and N atoms is as follows: blue N(H) = protein-derived amine moiety; magenta C(H) = formaldehyde-derived carbon moiety; red N(H) = nucleic acid-derived amine moiety; and dark green = amide of exogenous gel monomer (e.g., acrylamide). (c) The delipidation process is shown after the anchoring of proteins directly to the new hydrogel lattice; nucleic acid anchoring is chiefly indirect via protein bridges, anchoring via EDC (1-ethyl-3-(3-dimethyl-aminopropyl) carbodiimide) for linking the 5-phosphate group to surrounding amines (125) (**Figure 2**), or polymer entanglement. Stringent delipidation with detergent can then proceed without the risk of extensive biomolecule loss or structural disruption. (d) Optical clearing, refractive index matching, and high-resolution volumetric imaging (through delipidized tissue) can now occur for reading out molecules replotted onto the new tissue-hydrogel coordinate system shown in green (23).

thus permissive of intact whole-organ imaging at high resolution (16). It was noted that the resulting hydrogel-tissue hybrid “expanded” upon lipid removal in aqueous solution but “did not cause net tissue deformation. . . [R]emaining secured in place were fine structural details” (16, p. 334) since the expansion could be reversed with a solution change. Other diverse strategies for reducing opacity of intact tissue had been explored for years (though with varying degrees of efficacy and versatility) (**Figure 3**), but transparency was not the only experimental leverage achieved with the hydrogel-tissue chemistry (HTC) approach; for example, the new hybrids were designed to be macromolecule permeant—enabling multiple rounds of molecular interrogation of preserved biomolecules (proteins and nucleic acids) that had been anchored into the new physical structure (16, 23, 125).

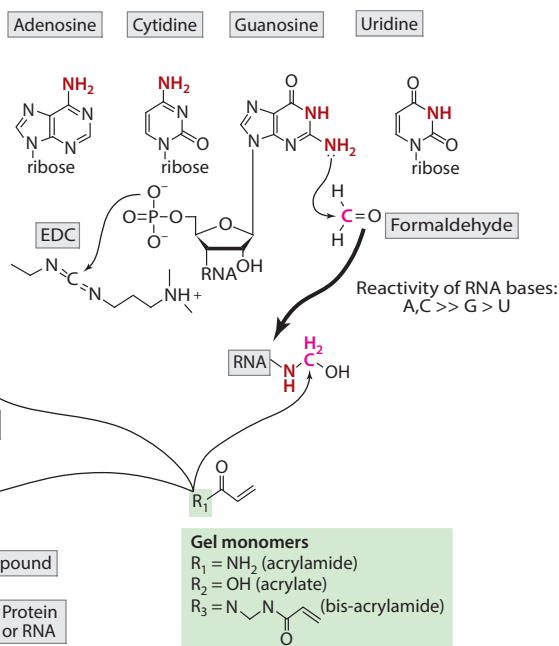
Single-photon confocal microscopy was initially used to image many-millimeter-thick blocks of the resulting clarified and fluorescently labeled human brain tissue, zebrafish central nervous systems, and whole adult mouse brain hemispheres (16). Diverse lines of work eventually emerged from this publication (23); as was noted therein, “infused elements need not be exclusively hydrogel monomers or acrylamide-based, and the properties of infused elements may be adjusted for varying degrees of clarity, rigidity, macromolecule-permeability or other functionality” (16, pp. 336–37). Also in 2013, a broad diversity of additional compositions, including those with acrylates or alginates, was described (25), and indeed variations and innovations on the theme rapidly emerged (**Figure 4**) (reviewed in 23, 53).

Also introduced was an electrophoretic tissue clearing (ETC) technique to accelerate lipid removal (16); lipid removal promotes tissue transparency and macromolecular interrogation, and this process can be carried out nondestructively after hydrogel-tissue hybrid formation (**Figure 1**). ETC employs electric field–forced clearance of lipid-containing ionic–detergent sodium dodecyl sulfate (SDS) micelles (**Figure 1**). Although helpful, ETC is not absolutely necessary to remove lipids, and the following year an ETC-independent approach was reported—passive CLARITY. This variant was initially described by Zhang et al. (147) and was found to be effective for adult central nervous systems and spinal cords. Passive CLARITY was soon thereafter reported to apply also to brain slices (104), and when combined with CLARITY-optimized light-sheet microscopy (COLM) this variant enabled imaging of entire adult mouse brains at subcellular resolution within several hours (131). At the same time, another CLARITY variant (PACT) was described (142), presenting modifications to the CLARITY reagents to passively achieve fast clearing of thick samples. After overnight tissue fixation in 4% paraformaldehyde (PFA), tissues were embedded in a 4% acrylamide hydrogel solution without the 4% PFA and 0.05% bisacrylamide of the original hydrogel formulation to minimize cross-linking (133, 142). In addition, a relatively inexpensive refractive index–matching solution, termed RIMS, was introduced (142).

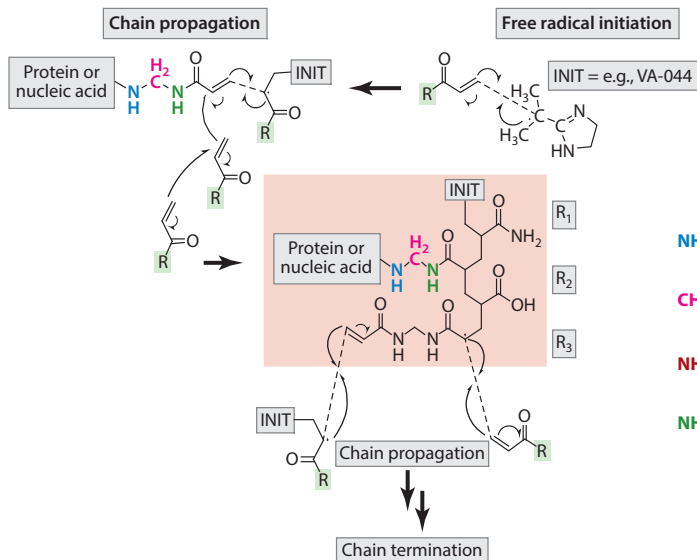
a Polypeptide functionalization



b Nucleic acid functionalization



c Tissue hydrogel formation



- NH_2 Amino group of nucleophilic small-molecule, peptide N-terminus, or amino acid side chain, e.g., lysine's ϵ -amine
- CH_2 Carbonyl carbon of cross-linking fixative, e.g., formaldehyde
- NH_2 Amino group or pyrimidine ring nitrogen of nucleic acids, e.g., adenosine, guanosine
- NH_2 Amide group of biomolecule-trapping gel monomer, e.g., acrylamide

(Caption appears on following page)

Figure 2 (Figure appears on preceding page)

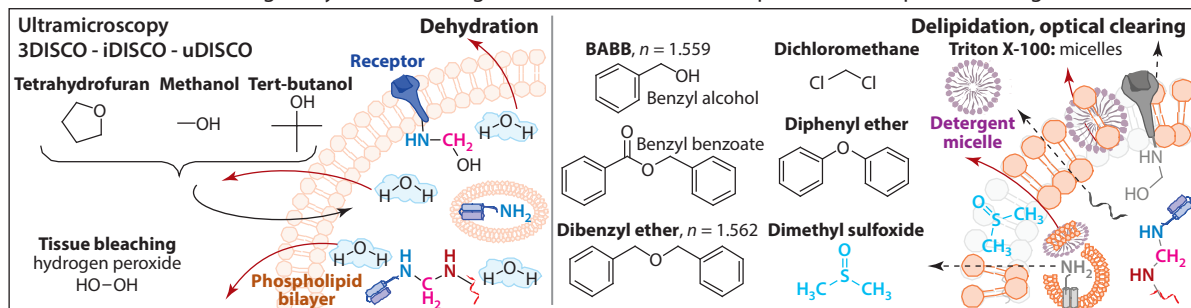
Example functionalization chemistry. Most current hydrogel-tissue chemistry (HTC) protocols include a preliminary biomolecule fixation step, such as aldehyde-based cross-linking of (a) proteins, peptides, and small-molecule amines and/or (b) nucleic acids, including targeted coupling of nucleic acids to the matrix via EDC (16, 125). (c) Biological macromolecule retention is next enhanced via creation and conjugation to (for example) an acrylamide-bisacrylamide gel matrix. Note that direct aromatic amine coupling of the RNA with aldehyde shown is expected to be a minor reaction compared to coupling reactions with protein aminomethylol moieties and compared to noncovalent caging of extensively crosslinked and protein-bound RNA in the hydrogel matrix. Depicted here are certain reactions as designed, but as Feldman pointed out 45 years ago, “The use of nucleic acid reactions with formaldehyde has outstripped our knowledge of their mode of action” (34, p. 2), and the same could be said of many modern tissue-based chemistries. A fundamental theme, however, is a gel monomer (*green box*, in this case showing three well-defined demonstrated R-moiety variants with the R1 acrylamide common to many current formulations) and the resulting tissue-hydrogel scaffold (here *peach box*, showing a representative HTC structure) into which the biological system is transformed; this provides the new coordinate system for replotting and jointly working with functionalized biomolecules stably in 3D space. Abbreviations: EDC, 1-ethyl-3-(3-dimethyl-aminopropyl) carbodiimide; INIT, free radical initiator.

The data of both Yang et al. (142) and Tomer et al. (131) in 2014 showed a moderate degree of tissue expansion associated with the HTC process, as had been described by Chung et al. (16) and indeed also as had been seen with earlier tissue clearing approaches (**Figure 5**). Although this effect had not been amplified to explore potential advantages, over the next two years, several HTC papers {11 [expansion microscopy (ExM) in 2015], 131 [expansion passive CLARITY technique (ePACT) in 2015], and 62 [magnified analysis of the proteome (MAP) in 2016]} soon enabled much-enhanced swelling of HTC hybrids to improve resolution of densely packed features. In a method unique for preserving endogenous fluorescence, ePACT (133) uses collagenase to enhance the magnitude of the size change. Two of the other versions, ExM (11, 30) and MAP (64), also embed tissue in a similar hydrogel network (reviewed in 53). In these formulations, which prescribe inclusion of acrylates (R2 in **Figure 2**) alongside acrylamide to enhance swelling (**Figures 2 and 4**), proteolysis can be carried out to facilitate this process but is not required. MAP additionally allows reversible expansion of the tissue-hydrogel hybrid (**Figure 5**) and super-resolution imaging of subcellular structures using high concentrations of acrylamide (30% acrylamide with 10% acrylate) to promote protein attachment to the hydrogel and prevent intra- and inter-protein cross-linking (64).

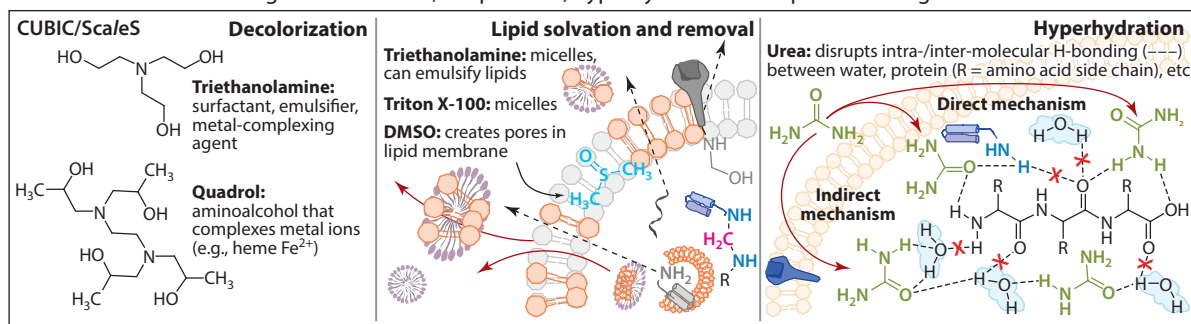
A large number of subsequent HTC studies put forward additional enhancements, including modifications of the ETC process and device (5, 59, 71, 72, 117, 121), of the hydrogel monomer and cross-linker levels (5, 32, 63, 131, 133, 142) and of other parameters while maintaining the basic hydrogel-tissue chemistry (18, 20, 22, 32, 63, 80, 84, 108, 122, 140, 142, 143, 145, 149). In addition to the acrylamide and/or acrylate-based PFA-coupled hydrogels noted above (PACT/ePACT, ExM, MAP), other gelation mechanisms have also been described. The SWITCH approach uses pH changes to synchronize formation of a glutaraldehyde-crosslinked matrix within tissue before CLARITY-type lipid removal via SDS, resulting in a heat- and chemical-resistant tissue-hydrogel hybrid that facilitates multiple rounds of labeling, elution, and relabeling (94, 106). Also described in the study that introduced PACT was a strategy termed PARS (perfusion-assisted agent release in situ) for whole-body clearing and labeling using perfusion through the vasculature to deliver hydrogel, clearing, labeling, and imaging reagents (133, 142). PACT and other passive CLARITY-based HTC methods were further adapted to tissues otherwise difficult or impossible to image intact, from the rigid and opaque bone [PACT-deCAL (133, 140) and Bone CLARITY (44)] to the soft and friable clinical samples and embryos (27, 51, 148).

In addition to small-molecule dyes, cellular stains, and protein labels (e.g., lectin) that can directly target proteins, DNA, and other biomolecules, tissues cleared using HTC can be stained using fluorescently tagged whole antibodies as well as smaller antibody formulations such as FAB

a Other forms of clearing: dehydration, detergent- and solvent-based delipidation and optical clearing



b Other forms of clearing: decolorization, delipidation, hyperhydration and optical clearing



NH₂ Amino group of nucleophilic small-molecule, peptide N-terminus, or amino acid side chain, e.g., lysine's ϵ -amine

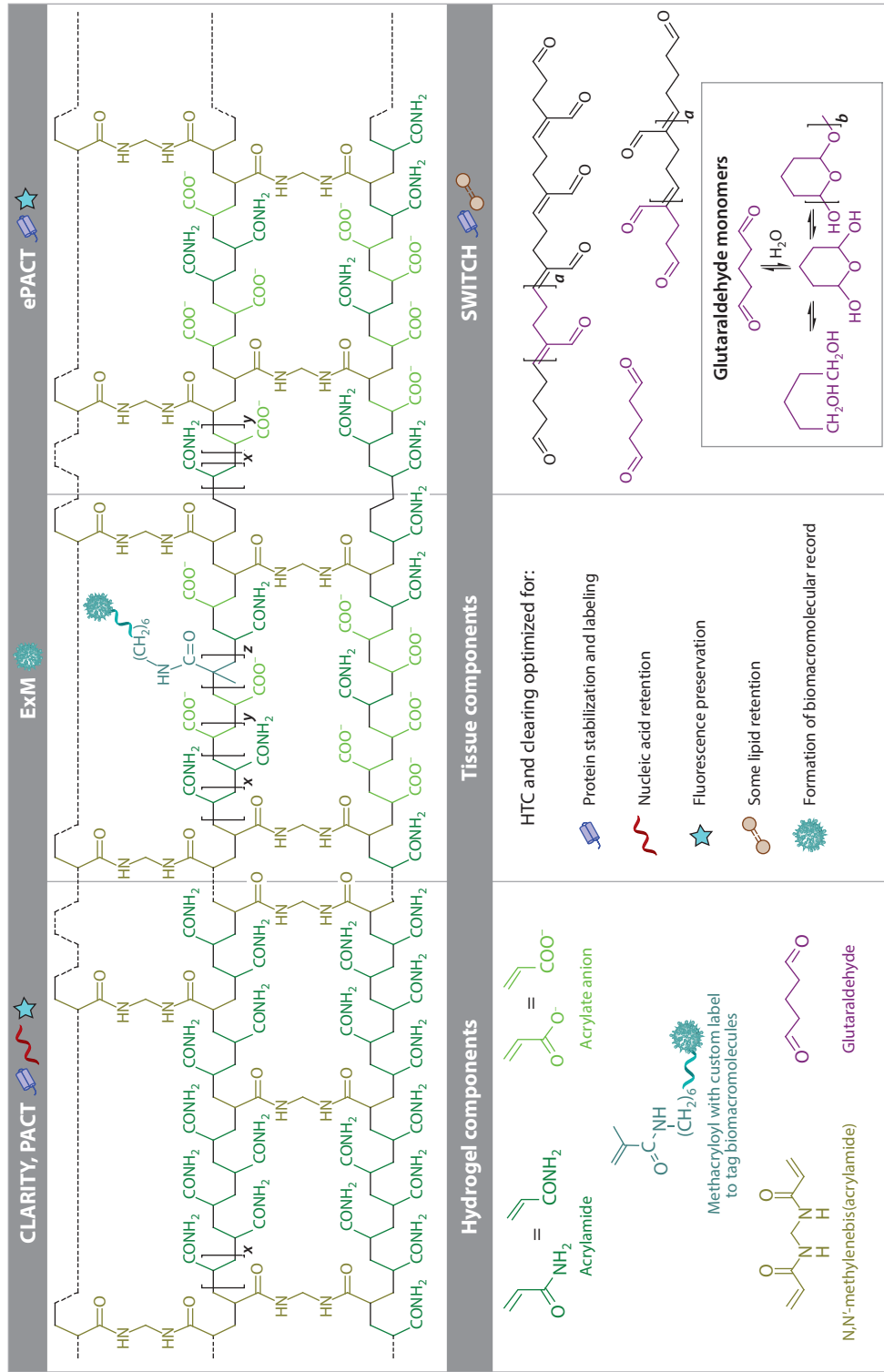
NH₂ Amino group or pyrimidine ring nitrogen of nucleic acids, e.g., adenosine, guanosine

CH₂ Carbonyl carbon of cross-linking fixative, e.g., formaldehyde

Figure 3

Non-hydrogel approaches for optical access to tissue. Beyond the hydrogel-tissue chemistry (HTC) concept, distinct transparency methods have been reported on the basis of various combinations of organic solvent-based dehydration and delipidation, or of hyperhydration-based optical clearing after less stringent permeabilization and delipidation steps. Unlike HTC constructs, these are all generally limited to optical imaging as the next and final step, rather than specifically enabling additional chemistry. The color code for tracking source of C and N atoms is as follows: blue N(H) = protein-derived amine moiety, magenta C(H) = formaldehyde-derived carbon moiety, red N(H) = nucleic acid-derived amine moiety. (a) Organic solvent-based clearing (dehydration, lipid removal, and refractive index matching) methods include BABB/ultramicroscopy (31), 3DISCO (33), iDISCO (107), FluoClearBABB (113), uDISCO (99), RetroDISCO (150), CRISTAL (57), and ethanol/ethyl cinnamate (61). (b) Aqueous-based clearing (refractive index matching, with optional hyperhydration and lipid removal) methods include: Scale and ScaleS (45, 46), SeeDB (56), CUBIC (65, 77, 123, 124, 126), 2,2'-thiodiethanol (TDE) (4, 18), FRUIT (49), ClearSee (66), acrylamide-free CLARITY (68, 81), sorbitol/sucrose/fructose (144), and single-cell optical clearing (21). Abbreviations: 3DISCO, 3-dimensional imaging of solvent-cleared organs; BABB, benzylalcohol/benzyl benzoate; CRISTAL, curing resin-infiltrated sample for transparent analysis with light; CUBIC, clear, unobstructed brain imaging cocktails and computational analysis; DMSO, dimethylsulfoxide; iDISCO, immunolabeling-enabled 3-DISCO; SeeDB, See Deep Brain; uDISCO, ultimate DISCO.


(fragment antigen-binding antibody) fragments (15, 16, 131, 133). Nanobodies were effective in staining PACT-cleared tissues (142); at 10% the size of full antibodies and stable over a variety of pH and temperature conditions, nanobodies are particularly appealing for labeling cleared thick tissues (133). The ETC process was accelerated using an approach called stochastic electrotransport (59), and an electrophoretically driven approach transported antibodies across a few millimeters of cleared tissue in less than an hour, approximately 800 times faster than via passive



(Caption appears on following page)

Figure 4 (Figure appears on preceding page)

Hydrogel-tissue hybrid backbone concepts. Hydrogel-tissue chemistry (HTC) structures involve integration of native biomolecules as part of the hydrogel framework as shown in **Figures 1** and **2**; for clarity on HTC subtypes, shown here are only the designs for exogenous chemical-derived backbones, while a fuller perspective with details on integration of native biomolecules appears as **Supplemental Figure 1**. HTC backbone formulations (a selected subset shown) allow customizable biological macromolecule anchoring and functionalization within a variety of frameworks. Molecular design of the initial backbone (*top left*; 16) and some of the subsequent early variants (*top middle, top right, bottom right*) are shown; color-coded backbone constituents are shown at lower left, and symbols for design properties of different methods are shown at bottom middle. The chemical backbone of the hydrogel built within the cells (*top left*) interacts with tissue elements through two principal routes: (i) covalent integration of amine-containing and otherwise functionalized proteins, nucleic acids, and small biomolecules; and (ii) noncovalent trapping of bulky moieties, such as extensively cross-linked protein networks within the hydrogel matrix. As with the initial HTC design, subsequent HTC variants are similarly capable of preserving molecular information during tissue processing through physically securing tissue macromolecules within the hydrogel or through recording their cellular location using custom labels that can withstand processing steps. Among the notable formulations, ExM (11), ePACT (133), and MAP (64) incorporate acrylate alongside acrylamide (as R2 of the R1, R2, and R3 moieties shown in **Figure 2**) into the basic HTC formulation to further enhance expansion. Bisacrylamide was not described in the initial PACT paper but can be included in the PACT formulation. SWITCH (94) gelation forgoes paraformaldehyde/acrylamide in favor of glutaraldehyde, a dialdehyde fixative that confers more robust protein cross-linking and some fixation of amine-containing phospholipids. EDC-CLARITY (125) provides a dedicated covalent-linkage pathway for more robust mRNA cross-linking to the tissue-hydrogel matrix. Other properties of interest seen with different variants include increased rigidity (seen with SWITCH) or conversely increased size-flexibility [as seen with PACT (142), ExM (11), ePACT (133), and with other methods not shown, including proExM (127), ExFISH (12), iExM (10), and MAP (64); **Supplemental Figure 1**]. Tissue components are critical constituents of the HTC backbone, as shown in more detail in **Supplemental Figure 1**; for example, in the top-row HTC methods, native proteins (with multiple reactive amines) can support cross-linking as well as bisacrylamide (R3 moiety of **Figure 2**) does. Moreover, native amines play a crucial role in catalyzing glutaraldehyde polymerization in the bottom right SWITCH method, in which low pH is used to initially slow down polymerization as glutaraldehyde is exposed to tissue amines until gel formation is desired. Abbreviations: EDC, 1-ethyl-3-(3-dimethyl-aminopropyl) carbodiimide; ePACT, expansion passive CLARITY technique; ExFISH, expansion fluorescent in situ hybridization; ExM, expansion microscopy; iExM, iterative expansion microscopy; MAP, magnified analysis of the proteome; PACT, passive CLARITY technique; proExM, protein-retention expansion microscopy; SWITCH, system-wide control of interaction time and kinetics of chemicals.

 Supplemental Material

diffusion (75). PRESTO (pressure-related efficient and stable transfer of macromolecules into organs) conferred increased antibody penetration depth and speed, particularly in cleared peripheral organs, by application of either centrifugal force or convection flow using a syringe pump during sample incubation in an antibody solution (71).

To broaden the types of macromolecular information obtained, recent studies have developed methods for visualizing lipids and RNA in HTC samples. Following earlier work that demonstrated the detection of endogenous mRNA in CLARITY specimens via standard in situ hybridization protocols (16), Yang et al. (142) showed that PACT hydrogels supported the use of single-molecule fluorescence in situ hybridization (smFISH) to detect individual mRNA transcripts at depth. In optimizing retention of RNA for labeling in cleared hydrogel-tissue hybrids, a carbodiimide compound [1-ethyl-3-(3-dimethyl-aminopropyl) carbodiimide (EDC)] was discovered to be useful for specifically linking RNA nucleotides directly to the tissue hydrogel (125) (**Figure 2**), and application of the hairpin chain reaction (HCR) amplification system facilitated multiplexed RNA labeling in these EDC-CLARITY samples that could be at least 3 mm thick. A 1% acrylamide hydrogel exhibited improved RNA labeling (for both total RNA and specifically mRNA) when compared to CLARITY samples (with 4% acrylamide) (125). Multiplexed single-molecule HCR was also demonstrated as an effective in situ hybridization technique in HTC brain slices embedded and cleared with PACT or ExM (12, 27, 115). Other methods led to improved visualization of fluorescent nanoparticles (polyethylene glycol-coated quantum dots) (116, 117), creation of nonfluorescent (dark) reaction products (horseradish peroxidase colorimetric labeling) (122), and development of lipophilic dyes that were altered to be aldehyde fixable to proteins to mark membranes even after HTC lipid removal (52).

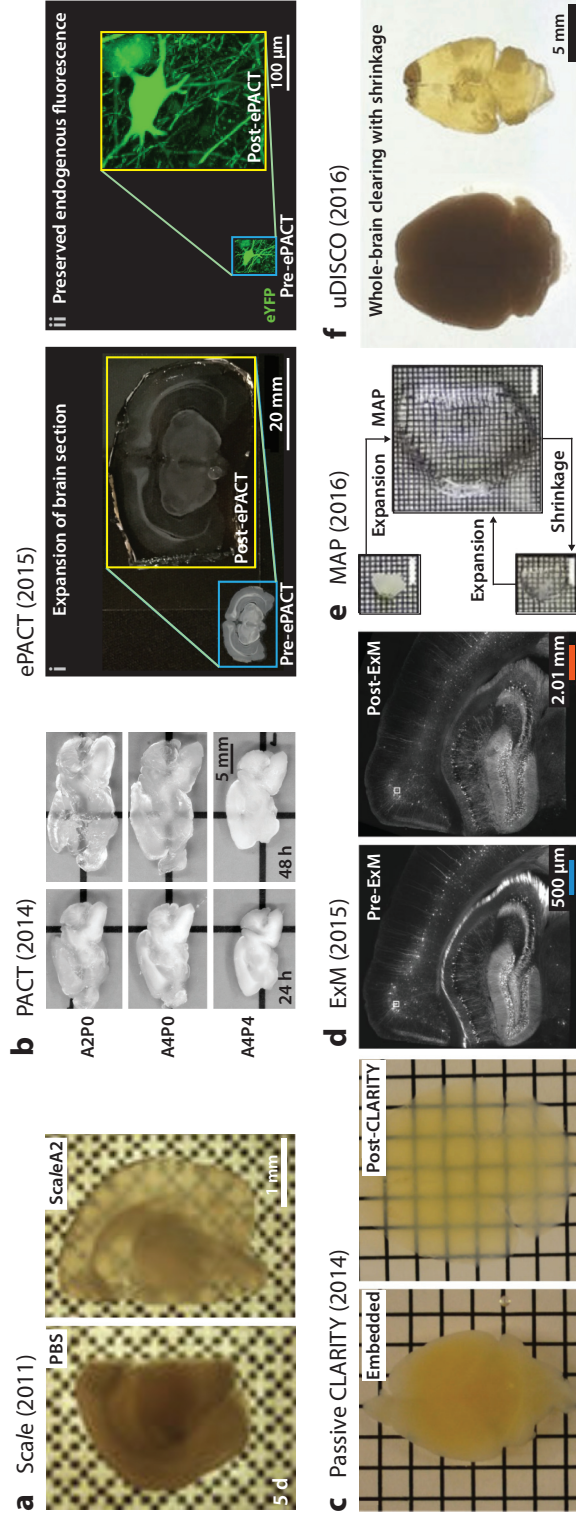


Figure 5

Examples of topology-preserving size changes. Size-adjustable tissue matrices can facilitate visualization of tissue architecture at the cellular or molecular level. The degree of intrinsic tissue-hydrogel expansion may be enhanced via the inclusion of yet more absorbent hydrogel monomers in the hydrogel-tissue chemistry (HTC) gel formulation. Expansion was seen with (a) the non-HTC method *Scale* in 2011 (46), (b) two HTC-based passive CLARITY techniques that preserve endogenous fluorescence during expansion: PACT in 2014 (142) and expansion-PACT (ePACT) in 2015 (133), and several additional HTC methods: (c) passive-CLARITY in 2014 (131), (d) expansion microscopy (ExM) in 2015 (11), and (e) magnified analysis of the proteome (MAP) in 2016 (64). By contrast, (f) the non-HTC organic solvent-based method uDISCO shrinks tissue (99). In (b) PACT/ePACT, mild enzymatic digestion followed by delipidation and hydration of the tissue-hydrogel matrix allows fourfold expansion with the preservation of biomolecular content and native fluorescence via expansion inversely proportional to the degree of hydrogel cross-linking; matrices of 2% acrylamide and no paraformaldehyde (A2P0) exhibited greatest expansion over delipidation (133). HTC methods have progressively achieved greater expansion of the tissue-hydrogel matrix [magnified analysis of the proteome (MAP): 5-fold expansion; iterative expansion microscopy (iExM): 20-fold expansion] via modified HTC, stringent temperature degradation of the tissue matrix, and/or alternate enzymatic digestion steps. However, increased hydrogel-tissue hybrid expansion for visualization tends to come at the cost of lost biomolecular content and reduced capability for ongoing functionalization, as well as reduced practicality for large-volume imaging. Images adapted as follows: (a) figure 1 of Hama et al. (46); (b) figure 1 of Yang et al. (142), supplemental figure 4 of Treweek et al. (133) and figure 2 of Treweek & Gradinaru (134); (c) supplemental figure 1 of Tomer et al. (131); (d) figure 3 of Chen et al. (11); (e) figure 1 of Ku et al. (64); (f) figure 1 of Pan et al. (99). Additional abbreviation: eYFP, enhanced yellow fluorescent protein.

HYDROGEL-TISSUE CHEMISTRY-BASED DISCOVERY IN NEUROSCIENCE AND THROUGHOUT THE ORGANISM

HTC methods have proven powerful for neuroscience; only a few examples of resulting discoveries are collected here to illustrate current capabilities and opportunities. First, a large number of studies have used the HTC approach to identify local and global wiring patterns of targeted neurons, beginning with the demonstration that a specific class of spinal cord neuron (NECAB expressing) exhibits midline crossing (147), and subsequently with the mapping of infection distribution for viral vectors microinjected into the lateral amygdala (LA) to analyze the neural mechanism of cocaine-cue memory engram formation in mice (50). Similarly, in a study analyzing the morphology of raphe-spinal fibers in the spinal cord, passive CLARITY provided visualization of a unique branching pattern of serotonergic fibers along the rostrocaudal axis as they extended toward the lateral motor neuron column (77, 78). Using rabies virus-based circuit mapping, passive CLARITY and COLM provided unbiased global mapping of all the neurons in the brain that project to dopamine neurons in the substantia nigra pars compacta, which in turn project to dorsolateral versus dorsomedial striatum (73). Likewise, rabies virus-based methods were used to trace monosynaptic inputs to projection-defined dopamine neurons via whole-brain CLARITY (in this case also with ETC and light-sheet imaging) (90). Anterograde tracing followed by CLARITY (using both ETC and passive clearing) provided visualization of synaptic targets of GABAergic projections from the medial septum (136). And in a study analyzing top-down control of anxiety and fear, passive CLARITY was used to track and map a distinct novel projection from ventromedial prefrontal cortex to basomedial amygdala (1). Integrating passive CLARITY with light-sheet microscopy and behavior, researchers implemented multiple-animal whole-brain activity mapping protocols for HTC alongside a strategy termed CAPTURE (143) for quantifying numbers and projections of behaviorally activated neurons.

PACT was used to study the distribution and morphology of astroglia in thick tissue sections (92) and the 3D distribution of multiple genetically defined neuron types in mouse brains (103). Passive CLARITY on sections of medial prefrontal cortex (mPFC) established the presence of nonoverlapping corticotropin-releasing factor and corticotropin-releasing factor receptor-1 circuits relevant to acute stress (138) and was used to map brain-wide viral expression in mice inoculated with western equine encephalitis virus in the foot pad (101). The distribution of microglia within the subventricular zone (a neurogenic region of the adult central nervous system) was mapped using passive CLARITY (38), and in the periventricular zone of the cerebellum, passive CLARITY was employed to analyze the organization of astrocytes during development (43). Passive CLARITY was used to show increased dendritic complexity in hippocampal pyramidal neurons of transgenic mice that exhibit enhanced learning (114) and to observe the localization of cells expressing neuromedin B, a bombesin-like neuropeptide that influences sighing behavior, around the facial nucleus, including the retrotrapezoid nucleus (a control center for breathing) (76). In transgenic mice using the nicotinic acetylcholine receptor $\alpha 2$ subunit (*Chrna2*) locus to mark deep-layer V Martinotti cells, passive CLARITY was used to verify labeling, specificity, and morphology of the targeted cells (47). For examining somatostatin-expressing interneurons in the dentate gyrus, CLARITY allowed demonstration of the axonal projections of a specific subset to the medial septum (146). Subcellular localization of a specific transcription factor, ESRRA, was analyzed using CLARITY (1% acrylamide with ETC) in brain sections (200 μm) to help elucidate the protein's role in cell signaling (111). Using viral vector tracing to label mPFC-projecting neurons in the basolateral amygdala (BLA), CLARITY provided visualization of the target specificity of those neurons, which aided in investigation of their role in manipulating fear associations (60). To analyze neuronal organization in the hypothalamus, whole-brain mapping of tyrosine

hydroxylase (TH)-positive neurons and projections was performed with CLARITY followed by immunostaining and COLM (109).

In addition to enabling these basic discoveries, HTC work has also stimulated technical and engineering advances. Passive CLARITY of electrolytically lesioned slices was used to correct electrode placement for fast-scan cyclic voltammetry (120) and to identify locations of implanted optical fibers (89). Following penetrating brain injury, passive CLARITY permitted brain-wide visualization of specific peptide accumulation in studies exploring targeted delivery of diagnostic and therapeutic compounds (86). And more broadly, body-wide biodistribution studies looking at chemicals or biologicals were found to benefit from HTC; for example, Treweek and coworkers (134) and Deverman et al. (28) demonstrated that whole-body PARS (142) could facilitate the generation of transduction maps of systemically delivered genes by adeno-associated viruses, which in turn facilitated characterization and discovery of new viral variants for targeting the central and peripheral nervous systems (8). HTC-based clearing has also technically enabled quadruple immunofluorescent staining as well as multiple rounds of labeling to reveal a variety of richly defined subcellular domains and molecule types in single human cerebellar sections (102).

Several studies have combined magnetic resonance imaging (MRI) with CLARITY. In probing the contribution of myelination to measurables from diffusion tensor imaging, passive CLARITY revealed that myelination correlates strongly with fractional anisotropy but only partially with radial diffusivity (9). The differential contributions of lipids and proteins to MRI contrast were analyzed using passive CLARITY to remove lipids and preserve proteins: Cleared tissues showed minimal contrast, increased relaxation times, and diffusion rates similar to free water, and lipids were thus demonstrated to be the dominant source of MRI contrast in brain tissue (74). In experimental autoimmune encephalomyelitis (a mouse model of multiple sclerosis), a direct relationship was defined between gray matter atrophy visualized using MRI and the number of axonal end bulbs in spinal cord visualized using passive CLARITY (118). This type of ground-truth work on clinical biomarkers is of immense and rapidly increasing value, particularly given the epidemiology of neurodegenerative diseases.

Disease model work in general has progressed rapidly with HTC. In a mouse model for Parkinson's disease, passive CLARITY revealed fragmented nigrostriatal axons (97). In addition to related studies in rat models (80, 119), direct human-disease HTC applications have also advanced rapidly. The effectiveness of CLARITY on postmortem human brain tissue was demonstrated using 500- μm thick tissue blocks from clinical autism samples that had been stored in formalin for over six years, revealing 3D morphologies not readily accessible using traditional sectioning (16). Similarly, passive CLARITY has been used to examine the 3D architecture of amyloid and tau aggregates in 500- μm thick banked tissue from Alzheimer's disease patients (3), and passive CLARITY has been used on 3-mm thick blocks of fresh or formalin-fixed tissue from Parkinson's disease patients to reveal Lewy body inclusions nearly 1 mm deep in the tissue (80).

NONNEURAL TISSUES

Although originally conceived for studying the brain (23, 24), the HTC approach can be extended to a wide variety of other organs and tissue types, including spinal cord, lung, heart, intestine, spleen, kidney, muscle, testis, pancreas, liver, skin, and bone (32, 44, 71, 72, 100, 140, 142). Its usefulness for imaging infection was demonstrated using PACT in mice infected with fluorescent *Mycobacterium tuberculosis*, which enabled visualization of 3D spatial distribution of bacteria throughout intact lungs (20). A modified PACT, MiPACT (for microbial identification after PACT) was designed to label bacterial rRNA (via HCR) for analysis of spatial organization and metabolic activity of bacteria in amorphous sputum samples from cystic fibrosis patients (27). Also

in lung, localization of nestin-expressing cells was observed throughout the vasculature (not the airway system) of tissue cleared via PACT, which motivated and guided investigation of the role of these cells in development of pulmonary hypertension (110). In a mouse model of lung adenocarcinoma, applying CLARITY to whole-lung tumors (clearing with two days of ETC) provided a comprehensive demonstration of significant differences in the cellular density and morphology of tumor cells with and without depletion of regulatory T cells (54). In pancreatic tissue, an evaluation of p53 loss of heterozygosity in tumor progression was enabled by HTC (95).

In liver, 3D positioning within the portal system (relative to the canals of Hering) was demonstrated using passive CLARITY for periportal hepatocytes, which undergo proliferation following injury (37). After application of passive CLARITY to rat kidneys, superresolution-STED microscopy revealed 3D positioning information at the nanometer scale (137). HTC on mouse and human gut tissue was achieved using passive CLARITY and immunostaining to visualize structures in the enteric nervous system, vasculature, smooth muscle layers, and epithelium, while also demonstrating compatibility with classical pathological stains such as hematoxylin-eosin and Heidenhain's Azan (96). Early systemic viral spread of human immunodeficiency virus 1 (HIV-1) in humanized mice was analyzed from gut-associated lymphoid tissues using PACT (58), and HTC (with ETC) was found useful for studying even dense and fibrous mouse hind-limb skeletal muscle tissue (91). In virgin and lactating mouse mammary glands, epithelial and tumor cells were made visible using PACT (82), whereas with passive CLARITY on intact mouse ovaries, the architecture and growth of ovarian follicles and their relationship to vasculature was analyzed throughout the mouse reproductive life (35, 83). Embryonic and neoplastic tissue analysis has been similarly optimized (48, 88, 132), and fast clearing was achieved by HTC in liver tissue (69) as well as in the growth plates of distal limbs (17).

In hatched chickens, adult *Xenopus*, and adult zebrafish, the comparative organization of HTC-stabilized cerebrospinal fluid-contacting cells revealed similarities pointing to a common bony vertebrate ancestor (141). Legs from chicken embryos were analyzed using passive CLARITY to reveal embryonic development of hallux positioning in the avian grasping foot (6). Passive CLARITY was also applied to the mouse nasal septum to visualize the morphology of horizontal basal cells in the olfactory epithelium following lesion of the olfactory bulb (112). The effect of subcutaneous injection of poly(methacrylic acid-co-methyl methacrylate) beads on vascularization was observed using passive CLARITY in mouse skin tissue (79). A dual-illumination-side light-sheet microscope optimized for imaging cardiac tissue over 1 cm³ in volume, combined with HTC, enabled researchers to measure ventricular dimensions, track the lineage of cardiac cells, and view the spatial distribution of cardiac-specific proteins within intact hearts (29). CLARITY also has been employed in intact mouse hearts as well as human heart tissue up to several millimeters thick (42, 62).

Host-pathogen interactions were studied using passive CLARITY and PACT to comprehensively examine morphology of necrotic granulomas from adult zebrafish infected with *Mycobacterium marinum* (19, 20). PACT and CUBIC (123) were found well suited for imaging the intact zebrafish testis at cellular resolution (39). Passive CLARITY was applied to transgenic *Xenopus* tadpoles to locate and quantify thyroid hormone signaling disruption by contaminants introduced during brain development (36). Applying passive CLARITY to the intact liver of lamprey undergoing metamorphosis provided visualization of the process of biliary degeneration, a process that occurs in human infants with biliary atresia via a mechanism that is still unknown (14), and passive CLARITY/COLM imaging in the lamprey was used to visualize the spatial organization of neuronal inputs and outputs in the optic tectum with the Neurobiotin tracer (55).

Addressing challenges beyond soft tissue, Bone CLARITY (44) was developed and applied along with a CLARITY-optimized light-sheet microscope to quantify marrow cells from cleared

adult intact mouse bones, revealing differences in fluorescent stem cell count and distribution after bone-forming agent administration (44). HTC approaches have been applied to multicellular plants as well via plant-enzyme-assisted (PEA)-CLARITY, an adaptation to perform optical clearing and antibody interrogation on plant tissues. Using cell wall-degrading enzymes to increase permeability and starch-hydrolyzing enzymes to improve transparency following passive clearing, PEA-CLARITY enabled visualization of fluorescent signals from expressed proteins as well as antibody staining in whole, intact tobacco and *Arabidopsis* leaves (98). The PEA-CLARITY protocol was later applied to study the 3D architecture of the *Medicago truncatula* root nodules (128).

OUTLOOK

The proven application domain of HTC in biology and medicine is rapidly expanding and has already resulted in numerous basic science discoveries and opportunities for clinical medicine (e.g., 24, 51, 143). However, the novelty of the preparation and its resulting data streams have created challenges. Here, we consider the current rate-limiting steps as well as opportunities for the future.

Early on, one of the clearest applications of the HTC approach was enabling high-resolution optical access to large intact tissues, organs, and organisms. Although this major goal was achieved, collecting high-resolution volumetric image data from large samples created new issues. For example, the transparency of the hydrogel-tissue hybrid allowed confocal or two-photon imaging over large volumes, but these slow point-scanning techniques led to bottlenecks in image acquisition (e.g., the collection of high-resolution structural data sets for an adult mouse brain required several days of imaging). Data collection on this timescale is associated with problems ranging from photobleaching to simple microscope overoccupancy, but rapid development of advanced light-sheet imaging, which offers orders-of-magnitude improvement in speed (29, 41, 44, 107, 115, 130, 131, 143), addressed this acquisition problem. Subsequent HTC-focused work included stochastic electrotransport (59); super-resolution-STED microscopy (137); adaptive optics (105); HTC sample handling chambers (44, 92, 93, 135); custom ETC and staining chambers (59, 71); and microfluidic chip-based embedding, clearing, and labeling (13).

The initial expansion found associated with HTC methods (16, 131, 142) was counteracted with size-normalization/contraction strategies during the refractive index-matching step to allow high-resolution objectives with limited working distance to access more of the brain (16). This strategy also had the effect of reducing the data set size, an important consideration for tractability. However, these considerations have become progressively less important with the advent of new hardware, including customized long-working-distance and high-resolution CLARITY objectives (87, 131) as well as distributed computing strategies.

Many studies have employed automated analysis pipelines for manipulating large CLARITY data sets; commercial 3D rendering software programs, such as Imaris or Arivis, can automate manually intensive data processing steps such as cell counting. Automation becomes even more valuable when analyzing thicker tissue sections or whole organs (44, 92, 143), but the utility of automated analysis extends beyond the domain of cell body recognition and counting. To quantify neural projection patterns, an automated method has been developed to compute 3D structure tensors from CLARITY images, and input of the tensors into diffusion tractography software yielded reconstruction of calculated streamlines mapped onto fibers from the CLARITY images (143). With this approach, connectivity between a seed region and specific downstream targets could be visualized and quantitatively evaluated by counting streamlines (143). In addition, alignment of autofluorescence images from multiple sample organs can be used to create a common reference space. When autofluorescence is combined with segmentation algorithms for automated cell detection, a transformation of the acquired signal from each sample onto this reference space

can be used to compare the regional distribution of labeled cells across brain samples and allow registration to public atlases, such as the Allen Brain Institute's Mouse Reference Atlas (90, 107, 143). Automatic annotation of CLARITY brain images (67) has been enabled by registering CLARITY brain images to the Allen atlas using a method called Mask-LDDMM. TeraFly is a free, open-source software tool designed specifically for 3D integrated visualization and annotation of massive, terabyte-sized image data sets like those acquired using the COLM system (7), and a manual segmentation tool (ManSegTool) for segmenting 3D neuronal data sets was demonstrated to enable neuroscientists to extract neurons from cerebellum slices cleared and imaged using passive CLARITY (85). For automatic annotation and standardization of brainwide data sets, WholeBrain is a free, open-source software that provides connectivity and activity-based mapping and quantification of multidimensional data, using a scale-invariant anatomical mouse brain atlas, which allows comparison of results across experiments and imaging platforms (40). Concurrently, an interactive Web-based framework, Openbrainmap (<http://openbrainmap.org>), was developed for data visualization and sharing between laboratories (40).

Tissue clarification is only one of many application domains of HTC methods, although it is arguably the most developed. Beyond tissue transparency, two studies have applied the hydrogel tissue-embedding step of CLARITY to stabilize mouse embryos or adult mouse brain tissue for micro-computed tomography (micro-CT) imaging using contrast agents that typically shrink tissue (2, 139). CLARITY was also used to reveal the 3D structure of patterned microtissues (129). And in stem cell-derived organoids, passive CLARITY followed by immunostaining was used to model and explore effects of cocaine exposure on the human fetal brain (70).

A final emerging domain of substantial interest, and an initial motivation for HTC (26), is the development of hydrogel-tissue hybrids with diverse types of functionalization, which would enable experiments extending far beyond static structural and molecular analysis. For example, creation of active constructs based on polymers with electrically conductive properties could allow new forms of interrogation of biological systems, and diverse additional forms of HTC and variants are in the process of emerging. Rooted in fundamental chemistry, the broad concept of envisioning (and remaking) metazoan animals and tissues as metareactants—that is, positionally intact and chemically versatile scaffolds of molecular reactants—may continue to open up new and unanticipated domains of investigation and discovery across diverse fields of biology.

DISCLOSURE STATEMENT

All protocols, software, and other information regarding these methods is freely available from the authors and online, and disseminated via free hands-on training courses (clarityresource-center.org and clover.caltech.edu). V.G. and K.D. have disclosed intellectual property regarding HTC methods to Caltech and Stanford, some of which has been licensed to ClearLight Diagnostics, which is exploring applications for cancer diagnostics, and with which there are consulting arrangements and equity; V.G. and K.D. each also have grant support from the US federal government (National Institutes of Health and National Science Foundation) to further develop, apply, and disseminate these methods.

ACKNOWLEDGMENTS

We thank Prof. Kwanghun Chung, Prof. Zhenan Bao, Dr. Ritchie Chen, Dr. Xiao Wang, Dr. Emily Sylwestrak, and members of our laboratories for helpful comments on the manuscript. K.D. is supported by the National Institutes of Health (NIH) R01DA03537701, R01MH075957, and R01MH086373, as well as by the Defense Advanced Research Projects Agency and Army

Research Laboratory NeuroFAST program (Cooperative Agreement W911NF-1420013). V.G. is supported by the NIH via the New Innovator Award DP2NS087949 and the Presidential Early Career Award for Science and Engineers, OT2OD023848-01, and R01AG047664; V.G. is also a Heritage Medical Research Institute Investigator and director of the Center for Molecular and Cellular Neuroscience in the Chen Institute at Caltech.

LITERATURE CITED

1. Adhikari A, Lerner TN, Finkelstein J, Pak S, Jennings JH, et al. 2015. Basomedial amygdala mediates top-down control of anxiety and fear. *Nature* 527:179–85
2. Anderson R, Maga AM. 2015. A novel procedure for rapid imaging of adult mouse brains with microCT using iodine-based contrast. *PLOS ONE* 10:e0142974
3. Ando K, Laborde Q, Lazar A, Godefroy D, Youssef I, et al. 2014. Inside Alzheimer brain with CLARITY: senile plaques, neurofibrillary tangles and axons in 3-D. *Acta Neuropathol.* 128:457–59
4. Aoyagi Y, Kawakami R, Osanai H, Hibi T, Nemoto T. 2015. A rapid optical clearing protocol using 2,2'-thiodiethanol for microscopic observation of fixed mouse brain. *PLOS ONE* 10:e0116280
5. Bastrup J, Larsen PH. 2017. Optimized CLARITY technique detects reduced parvalbumin density in a genetic model of schizophrenia. *J. Neurosci. Methods* 283:23–32
6. Botelho JF, Smith-Paredes D, Soto-Acuna S, Nunez-Leon D, Palma V, Vargas AO. 2017. Greater growth of proximal metatarsals in bird embryos and the evolution of hallux position in the grasping foot. *J. Exp. Zool. B Mol. Dev. Evol.* 328:106–18
7. Bria A, Iannello G, Onofri L, Peng H. 2016. TeraFly: real-time three-dimensional visualization and annotation of terabytes of multidimensional volumetric images. *Nat. Methods* 13:192–94
8. Chan KY, Jang MJ, Yoo BB, Greenbaum A, Ravi N, et al. 2017. Engineered AAVs for efficient noninvasive gene delivery to the central and peripheral nervous systems. *Nat. Neurosci.* 20:1172–79
9. Chang EH, Argyelan M, Aggarwal M, Chandon TS, Karlsgodt KH, et al. 2017. The role of myelination in measures of white matter integrity: combination of diffusion tensor imaging and two-photon microscopy of CLARITY intact brains. *Neuroimage* 147:253–61
10. Chang JB, Chen F, Yoon YG, Jung EE, Babcock H, et al. 2017. Iterative expansion microscopy. *Nat. Methods* 14:593–99
11. Chen F, Tillberg PW, Boyden ES. 2015. Expansion microscopy. *Science* 347:543
12. Chen F, Wassie AT, Cote AJ, Sinha A, Alon S, et al. 2016. Nanoscale imaging of RNA with expansion microscopy. *Nat. Methods* 13:679–84
13. Chen YY, Silva PN, Syed AM, Sindhvani S, Rocheleau JV, Chan WC. 2016. Clarifying intact 3D tissues on a microfluidic chip for high-throughput structural analysis. *PNAS* 113:14915–20
14. Chung-Davidson YW, Davidson PJ, Scott AM, Walaszczyk EJ, Brant CO, et al. 2014. A new clarification method to visualize biliary degeneration during liver metamorphosis in Sea Lamprey (*Petromyzon marinus*). *J. Vis. Exp.* 6:88
15. Chung K, Deisseroth K. 2013. CLARITY for mapping the nervous system. *Nat. Methods* 10:508–13
16. Chung K, Wallace J, Kim SY, Kalyanasundaram S, Andalman AS, et al. 2013. Structural and molecular interrogation of intact biological systems. *Nature* 497:332–37
17. Collette JC, Choubey L, Smith KM. 2017. Glial and stem cell expression of murine Fibroblast Growth Factor Receptor 1 in the embryonic and perinatal nervous system. *PeerJ* 5:e3519
18. Costantini I, Ghobril JP, Di Giovanna AP, Allegra Mascaro AL, Silvestri L, et al. 2015. A versatile clearing agent for multi-modal brain imaging. *Sci. Rep.* 5:9808
19. Cronan MR, Beerman RW, Rosenberg AF, Saelens JW, Johnson MG, et al. 2016. Macrophage epithelial reprogramming underlies mycobacterial granuloma formation and promotes infection. *Immunity* 45:861–76
20. Cronan MR, Rosenberg AF, Oehlers SH, Saelens JW, Sisk DM, et al. 2015. CLARITY and PACT-based imaging of adult zebrafish and mouse for whole-animal analysis of infections. *Dis. Model. Mech.* 8:1643–50

21. Cui Y, Wang X, Ren W, Liu J, Irudayaraj J. 2016. Optical clearing delivers ultrasensitive hyperspectral dark-field imaging for single-cell evaluation. *ACS Nano* 10:3132–43
22. d'Esposito A, Nikitichev D, Desjardins A, Walker-Samuel S, Lythgoe MF. 2015. Quantification of light attenuation in optically cleared mouse brains. *J. Biomed. Opt.* 20:80503
23. Deisseroth K. 2016. A look inside the brain. *Sci. Am.* 315:30–37
24. Deisseroth K. 2017. Optical and chemical discoveries recognized for impact on biology and psychiatry. *EMBO Rep.* 18:859–60
25. Deisseroth KA, Chung K. 2015. *Methods and compositions for preparing biological specimens for microscopic analysis*. www.google.com/patents/US20150144490. Filing date: March 13, 2013. US Patent Appl. No. US20150144490
26. Deisseroth KA, Gradinaru V. 2014. *Functional targeted brain endoskeletonization*. www.google.com/patents/US20140030192. Filing date: Jan 26, 2012. US Patent Appl. No. US20140030192
27. DePas WH, Starwalt-Lee R, Van Sambeek L, Ravindra Kumar S, Gradinaru V, Newman DK. 2016. Exposing the three-dimensional biogeography and metabolic states of pathogens in cystic fibrosis sputum via hydrogel embedding, clearing, and rRNA labeling. *mBio* 7:5e00796–16
28. Deverman BE, Pravdo PL, Simpson BP, Kumar SR, Chan KY, et al. 2016. Cre-dependent selection yields AAV variants for widespread gene transfer to the adult brain. *Nat. Biotech.* 34:204–9
29. Ding Y, Lee J, Ma J, Sung K, Yokota T, et al. 2017. Light-sheet fluorescence imaging to localize cardiac lineage and protein distribution. *Sci. Rep.* 7:42209
30. Dodt H-U. 2015. The superresolved brain. *Science* 347:474–75
31. Dodt H-U, Leischner U, Schierloh A, Jährling N, Mauch CP, et al. 2007. Ultramicroscopy: three-dimensional visualization of neuronal networks in the whole mouse brain. *Nat. Methods* 4:331–36
32. Epp JR, Niibori Y, Liz Hsiang HL, Mercaldo V, Deisseroth K, et al. 2015. Optimization of CLARITY for clearing whole-brain and other intact organs. *eNeuro* 2:1–15
33. Ertürk A, Becker K, Jährling N, Mauch CP, Hojer CD, et al. 2012. Three-dimensional imaging of solvent-cleared organs using 3DISCO. *Nat. Protoc.* 7:1983–95
34. Feldman MY. 1973. Reactions of nucleic acids and nucleoproteins with formaldehyde. *Prog. Nucl. Acid Res. Mol. Biol.* 13:1–49
35. Feng Y, Cui P, Lu X, Hsueh B, Möller Billig F, et al. 2017. CLARITY reveals dynamics of ovarian follicular architecture and vasculature in three-dimensions. *Sci. Rep.* 7:44810
36. Fini JB, Mughal BB, Le Mevel S, Leemans M, Lettmann M, et al. 2017. Human amniotic fluid contaminants alter thyroid hormone signalling and early brain development in *Xenopus* embryos. *Sci. Rep.* 7:43786
37. Font-Burgada J, Shalpour S, Ramaswamy S, Hsueh B, Rossell D, et al. 2015. Hybrid periportal hepatocytes regenerate the injured liver without giving rise to cancer. *Cell* 162:766–79
38. Fourgeaud L, Traves PG, Tufail Y, Leal-Bailey H, Lew ED, et al. 2016. TAM receptors regulate multiple features of microglial physiology. *Nature* 532:240–44
39. Fretaud M, Riviere L, Job E, Gay S, Lareyre JJ, et al. 2017. High-resolution 3D imaging of whole organ after clearing: taking a new look at the zebrafish testis. *Sci. Rep.* 7:43012
40. Fürth D, Vaissière T, Tzortzi O, Xuan Y, Martin A, et al. 2017. An interactive framework for whole-brain maps at cellular resolution. *Nat. Neurosci.* 21:139–49
41. Glaser AK, Reder NP, Chen Y, McCarty EF, Yin C, et al. 2017. Light-sheet microscopy for slide-free non-destructive pathology of large clinical specimens. *Nat. Biomed. Eng.* 1:0084
42. Gloschat CR, Koppel AC, Aras KK, Brennan JA, Holzem KM, Efimov IR. 2016. Arrhythmogenic and metabolic remodelling of failing human heart. *J. Physiol.* 594:3963–80
43. Gonzalez-Gonzalez MA, Gomez-Gonzalez GB, Becerra-Gonzalez M, Martinez-Torres A. 2017. Identification of novel cellular clusters define a specialized area in the cerebellar periventricular zone. *Sci. Rep.* 7:40768
44. Greenbaum A, Chan KY, Dobreva T, Brown D, Balani DH, et al. 2017. Bone CLARITY: clearing, imaging, and computational analysis of osteoprogenitors within intact bone marrow. *Sci. Transl. Med.* 9:387
45. Hama H, Hioki H, Namiki K, Hoshida T, Kurokawa H, et al. 2015. ScaleS: an optical clearing palette for biological imaging. *Nat. Neurosci.* 18:1518–29

46. Hama H, Kurokawa H, Kawano H, Ando R, Shimogori T, et al. 2011. Scale: a chemical approach for fluorescence imaging and reconstruction of transparent mouse brain. *Nat. Neurosci.* 14:1481–88
47. Hilscher MM, Leao RN, Edwards SJ, Leao KE, Kullander K. 2017. Chrna2–Martinotti cells synchronize layer 5 type A pyramidal cells via rebound excitation. *PLOS Biol.* 15:e2001392
48. Hirashima T, Adachi T. 2015. Procedures for the quantification of whole-tissue immunofluorescence images obtained at single-cell resolution during murine tubular organ development. *PLOS ONE* 10:e0135343
49. Hou B, Zhang D, Zhao S, Wei M, Yang Z, et al. 2015. Scalable and DiI-compatible optical clearance of the mammalian brain. *Front. Neuroanat* 9:19
50. Hsiang HL, Epp JR, van den Oever MC, Yan C, Rashid AJ, et al. 2014. Manipulating a “cocaine engram” in mice. *J. Neurosci.* 34:14115–27
51. Hsueh B, Burns VM, Pauerstein P, Holzem K, Ye L, et al. 2017. Pathways to clinical CLARITY: volumetric analysis of irregular, soft, and heterogeneous tissues in development and disease. *Sci. Rep.* 7:5899
52. Jensen KHR, Berg RW. 2016. CLARITY-compatible lipophilic dyes for electrode marking and neuronal tracing. *Sci. Rep.* 6:32674
53. Jensen KHR, Berg RW. 2017. Advances and perspectives in tissue clearing using CLARITY. *J. Chem. Neuroanat.* 86:19–34
54. Joshi NS, Akama-Garren EH, Lu Y, Lee DY, Chang GP, et al. 2015. Regulatory T cells in tumor-associated tertiary lymphoid structures suppress anti-tumor T cell responses. *Immunity* 43:579–90
55. Kardamakis AA, Pérez-Fernández J, Grillner S. 2016. Spatiotemporal interplay between multisensory excitation and recruited inhibition in the lamprey optic tectum. *eLife* 5:e16472
56. Ke MT, Fujimoto S, Imai T. 2013. SeeDB: a simple and morphology-preserving optical clearing agent for neuronal circuit reconstruction. *Nat. Neurosci.* 16:1154–61
57. Kellner M, Heidrich M, Lorbeer RA, Antonopoulos GC, Knudsen L, et al. 2016. A combined method for correlative 3D imaging of biological samples from macro to nano scale. *Sci. Rep.* 6:35606
58. Kieffer C, Ladinsky MS, Ninh A, Galimidi RP, Bjorkman PJ. 2017. Longitudinal imaging of HIV-1 spread in humanized mice with parallel 3D immunofluorescence and electron tomography. *eLife* 6:e23282
59. Kim S-Y, Cho JH, Murray E, Bakh N, Choi H, et al. 2015. Stochastic electrotransport selectively enhances the transport of highly electromobile molecules. *PNAS* 112:E6274–83
60. Klavir O, Prigge M, Sarel A, Paz R, Yizhar O. 2017. Manipulating fear associations via optogenetic modulation of amygdala inputs to prefrontal cortex. *Nat. Neurosci.* 20:836–44
61. Klingberg A, Hasenberg A, Ludwig-Portugall I, Medyukhina A, Mann L, et al. 2017. Fully automated evaluation of total glomerular number and capillary tuft size in nephritic kidneys using lightsheet microscopy. *J. Am. Soc. Nephrol.* 28:452–59
62. Kolesova H, Capek M, Radochova B, Janacek J, Sedmera D. 2016. Comparison of different tissue clearing methods and 3D imaging techniques for visualization of GFP-expressing mouse embryos and embryonic hearts. *Histochem. Cell Biol.* 146:141–52
63. Krolewski DM, Kumar V, Martin B, Tomer R, Deisseroth K, et al. 2018. Quantitative validation of immunofluorescence and lectin staining using reduced CLARITY acrylamide formulations. *Brain Struct. Funct.* 223:987–99
64. Ku T, Swaney J, Park JY, Albanese A, Murray E, et al. 2016. Multiplexed and scalable super-resolution imaging of three-dimensional protein localization in size-adjustable tissues. *Nat. Biotechnol.* 34:973–81
65. Kubota SI, Takahashi K, Nishida J, Morishita Y, Ehata S, et al. 2017. Whole-body profiling of cancer metastasis with single-cell resolution. *Cell Rep.* 20:236–50
66. Kurihara D, Mizuta Y, Sato Y, Higashiyama T. 2015. ClearSee: a rapid optical clearing reagent for whole-plant fluorescence imaging. *Development* 142:4168–79
67. Kутten KS, Vogelstein JT, Charon N, Ye L, Deisseroth K, Miller MI. 2016. *Deformably registering and annotating whole CLARITY brains to an atlas via masked LDDMM*. Presented at Proc. SPIE Opt., Photonics, Digit. Technol. for Imaging Appl. IV, Brussels, Belg.
68. Lai HM, Liu AKL, Ng W-L, DeFelice J, Lee WS, et al. 2016. Rationalisation and validation of an acrylamide-free procedure in three-dimensional histological imaging. *PLOS ONE* 11:e0158628

69. Lai M, Li X, Li J, Hu Y, Czajkowsky DM, Shao Z. 2017. Improved clearing of lipid droplet-rich tissues for three-dimensional structural elucidation. *Acta Biochim. Biophys. Sin.* 49:465–67
70. Lee CT, Chen J, Kindberg AA, Bendriem RM, Spivak CE, et al. 2017. CYP3A5 mediates effects of cocaine on human neocortico genesis: studies using an in vitro 3D self-organized hPSC model with a single cortex-like unit. *Neuropsychopharmacology* 42:774–84
71. Lee E, Choi J, Jo Y, Kim JY, Jang YJ, et al. 2016. ACT-PRESTO: rapid and consistent tissue clearing and labeling method for 3-dimensional (3D) imaging. *Sci. Rep.* 6:18631
72. Lee H, Park JH, Seo I, Park SH, Kim S. 2014. Improved application of the electrophoretic tissue clearing technology, CLARITY, to intact solid organs including brain, pancreas, liver, kidney, lung, and intestine. *BMC Dev. Biol.* 14:48
73. Lerner TN, Shilyansky C, Davidson TJ, Evans KE, Beier KT, et al. 2015. Intact-brain analyses reveal distinct information carried by SNc dopamine subcircuits. *Cell* 162:635–47
74. Leuze C, Aswendt M, Ferenczi E, Liu CW, Hsueh B, et al. 2017. The separate effects of lipids and proteins on brain MRI contrast revealed through tissue clearing. *Neuroimage* 156:412–22
75. Li J, Czajkowsky DM, Li X, Shao Z. 2015. Fast immuno-labeling by electrophoretically driven infiltration for intact tissue imaging. *Sci. Rep.* 5:10640
76. Li P, Janczewski WA, Yackle K, Kam K, Pagliardini S, et al. 2016. The peptidergic control circuit for sighing. *Nature* 530:293–97
77. Liang H, Schofield E, Paxinos G. 2016. Imaging serotonergic fibers in the mouse spinal cord using the CLARITY/CUBIC technique. *J. Vis. Exp.* 108:53673
78. Liang H, Wang S, Francis R, Whan R, Watson C, Paxinos G. 2015. Distribution of raphespinal fibers in the mouse spinal cord. *Mol. Pain* 11:42
79. Lisovsky A, Zhang DK, Sefton MV. 2016. Effect of methacrylic acid beads on the sonic hedgehog signaling pathway and macrophage polarization in a subcutaneous injection mouse model. *Biomaterials* 98:203–14
80. Liu AKL, Hurry MED, Ng OTW, DeFelice J, Lai HM, et al. 2016. Bringing CLARITY to the human brain: visualization of Lewy pathology in three dimensions. *Neuropathol. Appl. Neurobiol.* 42:573–87
81. Liu AKL, Lai HM, Chang RCC, Gentleman SM. 2017. Free of acrylamide sodium dodecyl sulphate (SDS)-based tissue clearing (FASTClear): a novel protocol of tissue clearing for three-dimensional visualization of human brain tissues. *Neuropathol. Appl. Neurobiol.* 43:346–51
82. Lloyd-Lewis B, Davis FM, Harris OB, Hitchcock JR, Lourenco FC, et al. 2016. Imaging the mammary gland and mammary tumours in 3D: optical tissue clearing and immunofluorescence methods. *Breast Cancer Res.* 18:127
83. Lu X, Guo S, Cheng Y, Kim J-h, Feng Y, Feng Y. 2017. Stimulation of ovarian follicle growth after AMPK inhibition. *Reproduction* 153:683–94
84. Magliaro C, Callara AL, Mattei G, Morcinelli M, Viaggi C, et al. 2016. Clarifying CLARITY: quantitative optimization of the diffusion based delipidation protocol for genetically labeled tissue. *Front. Neurosci.* 10:179
85. Magliaro C, Callara AL, Vanello N, Ahluwalia A. 2017. A manual segmentation tool for three-dimensional neuron datasets. *Front. Neuroinform.* 11:36
86. Mann AP, Scodeller P, Hussain S, Joo J, Kwon E, et al. 2016. A peptide for targeted, systemic delivery of imaging and therapeutic compounds into acute brain injuries. *Nat. Commun.* 7:11980
87. Marx V. 2014. Microscopy: seeing through tissue. *Nat. Methods* 11:1209–14
88. Mayrhofer M, Gourain V, Reischl M, Affaticati P, Jenett A, et al. 2017. A novel brain tumour model in zebrafish reveals the role of YAP activation in MAPK- and PI3K-induced malignant growth. *Dis. Model. Mech.* 10:15–28
89. Menegas W, Babayan BM, Uchida N, Watabe-Uchida M. 2017. Opposite initialization to novel cues in dopamine signaling in ventral and posterior striatum in mice. *eLife* 6:e21886
90. Menegas W, Bergan JF, Ogawa SK, Isogai Y, Umadevi Venkataraju K, et al. 2015. Dopamine neurons projecting to the posterior striatum form an anatomically distinct subclass. *eLife* 4:e10032
91. Milgroom A, Ralston E. 2016. Clearing skeletal muscle with CLARITY for light microscopy imaging. *Cell Biol. Int.* 40:478–83

92. Miller SJ, Rothstein JD. 2016. Astroglia in thick tissue with super resolution and cellular reconstruction. *PLOS ONE* 11:e0160391
93. Miller SJ, Rothstein JD. 2017. 3D printer generated tissue iMolds for cleared tissue using single- and multi-photon microscopy for deep tissue evaluation. *Biol. Proced. Online* 19:7
94. Murray E, Cho JH, Goodwin D, Ku T, Swaney J, et al. 2015. Simple, scalable proteomic imaging for high-dimensional profiling of intact systems. *Cell* 163:1500–14
95. Muzumdar MD, Dorans KJ, Chung KM, Robbins R, Tammela T, et al. 2016. Clonal dynamics following p53 loss of heterozygosity in *Kras*-driven cancers. *Nat. Commun.* 7:12685
96. Neckel PH, Mattheus U, Hirt B, Just L, Mack AF. 2016. Large-scale tissue clearing (PACT): technical evaluation and new perspectives in immunofluorescence, histology, and ultrastructure. *Sci. Rep.* 6:34331
97. Nordströma U, Beauvais G, Ghosh A, Pulikkaparambil Sasidharan BC, Lundblad M, et al. 2015. Progressive nigrostriatal terminal dysfunction and degeneration in the engrailed1 heterozygous mouse model of Parkinson's disease. *Neurobiol. Dis.* 73:70–82
98. Palmer WM, Martin AP, Flynn JR, Reed SL, White RG, et al. 2015. PEA-CLARITY: 3D molecular imaging of whole plant organs. *Sci. Rep.* 5:13492
99. Pan C, Cai R, Quacquarelli FP, Ghasemigharagoz A, Lourbopoulos A, et al. 2016. Shrinkage-mediated imaging of entire organs and organisms using uDISCO. *Nat. Methods* 13:859–67
100. Pan M, Reid MA, Lowman XH, Kulkarni RP, Tran TQ, et al. 2016. Regional glutamine deficiency in tumours promotes dedifferentiation through inhibition of histone demethylation. *Nat. Cell Biol.* 18:1090–101
101. Phillips AT, Rico AB, Stauff CB, Hammond SL, Aboellail TA, et al. 2016. Entry sites of Venezuelan and western equine encephalitis viruses in the mouse central nervous system following peripheral infection. *J. Virol.* 90:5785–96
102. Phillips J, Laude A, Lightowers R, Morris CM, Turnbull DM, Lax NZ. 2016. Development of passive CLARITY and immunofluorescent labelling of multiple proteins in human cerebellum: understanding mechanisms of neurodegeneration in mitochondrial disease. *Sci. Rep.* 6:26013
103. Plummer NW, Evsyukova IY, Robertson SD, de Marchena J, Tucker CJ, Jensen P. 2015. Expanding the power of recombinase-based labeling to uncover cellular diversity. *Development* 142:4385–93
104. Poguzhelskaya E, Artamonov D, Bolshakova A, Vlasova O, Bezprozvanny I. 2014. Simplified method to perform CLARITY imaging. *Mol. Neurodegener.* 9:19
105. Reinig MR, Novak SW, Tao X, Bentolila LA, Roberts DG, et al. 2016. Enhancing image quality in cleared tissue with adaptive optics. *J. Biomed. Opt.* 21:121508
106. Ren J, Choi H, Chung K, Bouma BE. 2017. Label-free volumetric optical imaging of intact murine brains. *Sci. Rep.* 7:46306
107. Renier N, Wu Z, Simon DJ, Yang J, Ariel P, Tessier-Lavigne M. 2014. iDISCO: a simple, rapid method to immunolabel large tissue samples for volume imaging. *Cell* 159:896–910
108. Roberts DG, Johnsonbaugh HB, Spence RD, MacKenzie-Graham A. 2016. Optical clearing of the mouse central nervous system using passive CLARITY. *J. Vis. Exp.* 112:e54025
109. Romanov RA, Zeisel A, Bakker J, Girach F, Hellysaz A, et al. 2017. Molecular interrogation of hypothalamic organization reveals distinct dopamine neuronal subtypes. *Nat. Neurosci.* 20:176–88
110. Saboor F, Reckmann AN, Tomczyk CU, Peters DM, Weissmann N, et al. 2016. Nestin-expressing vascular wall cells drive development of pulmonary hypertension. *Eur. Respir. J.* 47:876–88
111. Saul MC, Seward CH, Troy JM, Zhang H, Sloofman LG, et al. 2017. Transcriptional regulatory dynamics drive coordinated metabolic and neural response to social challenge in mice. *Genome Res.* 27:959–72
112. Schnittke N, Herrick DB, Lin B, Peterson J, Coleman JH, et al. 2015. Transcription factor p63 controls the reserve status but not the stemness of horizontal basal cells in the olfactory epithelium. *PNAS* 112:E5068–77
113. Schwarz MK, Scherbarth A, Sprengel R, Engelhardt J, Theer P, Giese G. 2015. Fluorescent-protein stabilization and high-resolution imaging of cleared, intact mouse brains. *PLOS ONE* 10:e0124650
114. Serita T, Fukushima H, Kida S. 2017. Constitutive activation of CREB in mice enhances temporal association learning and increases hippocampal CA1 neuronal spine density and complexity. *Sci. Rep.* 7:42528

115. Shah S, Lubeck E, Schwarzkopf M, He TF, Greenbaum A, et al. 2016. Single-molecule RNA detection at depth by hybridization chain reaction and tissue hydrogel embedding and clearing. *Development* 143:2862–67
116. Sindhvani S, Syed AM, Wilhelm S, Chan WC. 2017. Exploring passive clearing for 3D optical imaging of nanoparticles in intact tissues. *Bioconjug. Chem.* 28:253–59
117. Sindhvani S, Syed AM, Wilhelm S, Glancy DR, Chen YY, et al. 2016. Three-dimensional optical mapping of nanoparticle distribution in intact tissues. *ACS Nano* 10:5468–78
118. Spence RD, Kurth F, Itoh N, Mongerson CR, Wailes SH, et al. 2014. Bringing CLARITY to gray matter atrophy. *Neuroimage* 101:625–32
119. Stefaniuk M, Gualda EJ, Pawlowska M, Legutko D, Matryba P, et al. 2016. Light-sheet microscopy imaging of a whole cleared rat brain with Thy1-GFP transgene. *Sci. Rep.* 6:28209
120. Stout KA, Dunn AR, Lohr KM, Alter SP, Cliburn RA, et al. 2016. Selective enhancement of dopamine release in the ventral pallidum of methamphetamine-sensitized mice. *ACS Chem. Neurosci.* 7:1364–73
121. Sulkin MS, Widder E, Shao C, Holzem KM, Gloschat C, et al. 2013. Three-dimensional printing physiology laboratory technology. *Am. J. Physiol. Heart Circ. Physiol.* 305:H1569–73
122. Sung K, Ding Y, Ma J, Chen H, Huang V, et al. 2016. Simplified three-dimensional tissue clearing and incorporation of colorimetric phenotyping. *Sci. Rep.* 6:30736
123. Susaki EA, Tainaka K, Perrin D, Kishino F, Tawara T, et al. 2014. Whole-brain imaging with single-cell resolution using chemical cocktails and computational analysis. *Cell* 157:726–39
124. Susaki EA, Tainaka K, Perrin D, Yukinaga H, Kuno A, Ueda HR. 2015. Advanced CUBIC protocols for whole-brain and whole-body clearing and imaging. *Nat. Protoc.* 10:1709–27
125. Sylwestrak EL, Rajasethupathy P, Wright MA, Jaffe A, Deisseroth K. 2016. Multiplexed intact-tissue transcriptional analysis at cellular resolution. *Cell* 164:792–804
126. Tainaka K, Kubota SI, Suyama TQ, Susaki EA, Perrin D, et al. 2014. Whole-body imaging with single-cell resolution by tissue decolorization. *Cell* 159:911–24
127. Tillberg PW, Chen F, Piatkevich KD, Zhao Y, Yu C-C, et al. 2016. Protein-retention expansion microscopy of cells and tissues labeled using standard fluorescent proteins and antibodies. *Nat. Biotechnol.* 34:987–92
128. Timmers AC. 2016. Light microscopy of whole plant organs. *J. Microsc.* 263:165–70
129. Todhunter ME, Jee NY, Hughes AJ, Coyle MC, Cerchiari A, et al. 2015. Programmed synthesis of three-dimensional tissues. *Nat. Methods* 12:975–81
130. Tomer R, Lovett-Barron M, Kauvar I, Andalman A, Burns VM, et al. 2015. SPED light sheet microscopy: fast mapping of biological system structure and function. *Cell* 163:1796–806
131. Tomer R, Ye L, Hsueh B, Deisseroth K. 2014. Advanced CLARITY for rapid and high-resolution imaging of intact tissues. *Nat. Protoc.* 9:1682–97
132. Tran E, Hellebust A, Wu J, Gillenwater A, Vigneswaran N, Richards-Kortum RR. 2016. *Optically cleared mouse tongues for three-dimensional investigation of oral neoplasia*. Presented at Optical Tomogr. Spectrosc., Fort Lauderdale, FL
133. Treweek JB, Chan KY, Flytzanis NC, Yang B, Deverman BE, et al. 2015. Whole-body tissue stabilization and selective extractions via tissue-hydrogel hybrids for high-resolution intact circuit mapping and phenotyping. *Nat. Protoc.* 10:1860–96
134. Treweek JB, Gradinaru V. 2016. Extracting structural and functional features of widely distributed biological circuits with single cell resolution via tissue clearing and delivery vectors. *Curr. Opin. Biotechnol.* 40:193–207
135. Tyson AL, Hilton ST, Andraea LC. 2015. Rapid, simple and inexpensive production of custom 3D printed equipment for large-volume fluorescence microscopy. *Int. J. Pharm.* 494:651–56
136. Unal G, Joshi A, Viney TJ, Kis V, Somogyi P. 2015. Synaptic targets of medial septal projections in the hippocampus and extrahippocampal cortices of the mouse. *J. Neurosci.* 35:15812–26
137. Unnersjo-Jess D, Scott L, Blom H, Brismar H. 2016. Super-resolution stimulated emission depletion imaging of slit diaphragm proteins in optically cleared kidney tissue. *Kidney Int.* 89:243–47
138. Uribe-Marino A, Gassen NC, Wiesbeck MF, Balsevich G, Santarelli S, et al. 2016. Prefrontal cortex corticotropin-releasing factor receptor 1 conveys acute stress-induced executive dysfunction. *Biol. Psychiatry* 80:743–53

139. Wong MD, Spring S, Henkelman RM. 2014. Structural stabilization of tissue for embryo phenotyping using micro-CT with iodine staining. *PLOS ONE* 8:e84321
140. Woo J, Lee M, Seo JM, Park HS, Cho YE. 2016. Optimization of the optical transparency of rodent tissues by modified PACT-based passive clearing. *Exp. Mol. Med.* 48:e274
141. Xavier AL, Fontaine R, Bloch S, Affaticati P, Jenett A, et al. 2017. Comparative analysis of monoaminergic cerebrospinal fluid-contacting cells in Osteichthyes (bony vertebrates). *J. Comp. Neurol.* 525:2265–83
142. Yang B, Treweek JB, Kulkarni RP, Deverman BE, Chen CK, et al. 2014. Single-cell phenotyping within transparent intact tissue through whole-body clearing. *Cell* 158:945–58
143. Ye L, Allen WE, Thompson KR, Tian Q, Hsueh B, et al. 2016. Wiring and molecular features of prefrontal ensembles representing distinct experiences. *Cell* 165:1776–88
144. Yu T, Qi Y, Wang J, Feng W, Xu J, et al. 2016. Rapid and Prodim iodide-compatible optical clearing method for brain tissue based on sugar/sugar-alcohol. *J. Biomed. Opt.* 21:081203
145. Yu T, Qi Y, Zhu J, Xu J, Gong H, et al. 2017. Elevated-temperature-induced acceleration of PACT clearing process of mouse brain tissue. *Sci. Rep.* 7:38848
146. Yuan M, Meyer T, Benkowitz C, Savanthrapadian S, Ansel-Bollepalli L, et al. 2017. Somatostatin-positive interneurons in the dentate gyrus of mice provide local- and long-range septal synaptic inhibition. *eLife* 6:e21105
147. Zhang MD, Tortoriello G, Hsueh B, Tomer R, Ye L, et al. 2014. Neuronal calcium-binding proteins 1/2 localize to dorsal root ganglia and excitatory spinal neurons and are regulated by nerve injury. *PNAS* 111:E1149–58
148. Zhao Y, Bucur O, Irshad H, Chen F, Weins A, et al. 2017. Nanoscale imaging of clinical specimens using pathology-optimized expansion microscopy. *Nat. Biotechnol.* 35:757–64
149. Zheng H, Rinaman L. 2016. Simplified CLARITY for visualizing immunofluorescence labeling in the developing rat brain. *Brain Struct. Funct.* 221:2375–83
150. Zygelyte E, Bernard ME, Tomlinson JE, Martin MJ, Terhorst A, et al. 2016. RetroDISCO: clearing technique to improve quantification of retrograde labeled motor neurons of intact mouse spinal cords. *J. Neurosci. Methods* 271:34–42

Contents

Structural Basis for G Protein–Coupled Receptor Signaling <i>Sarah C. Erlandson, Conor McMabon, and Andrew C. Kruse</i>	1
Collapse Transitions of Proteins and the Interplay Among Backbone, Sidechain, and Solvent Interactions <i>Alex S. Holehouse and Robit V. Pappu</i>	19
Measuring Entropy in Molecular Recognition by Proteins <i>A. Joshua Wand and Kim A. Sharp</i>	41
Assembly of COPI and COPII Vesicular Coat Proteins on Membranes <i>Julien Bébune and Felix T. Wieland</i>	63
Imaging mRNA In Vivo, from Birth to Death <i>Evelina Tutucci, Nathan M. Livingston, Robert H. Singer, and Bin Wu</i>	85
Nanodiscs: A Controlled Bilayer Surface for the Study of Membrane Proteins <i>Mark A. McLean, Michael C. Gregory, and Stephen G. Sligar</i>	107
The Jigsaw Puzzle of mRNA Translation Initiation in Eukaryotes: A Decade of Structures Unraveling the Mechanics of the Process <i>Yaser Hashem and Joachim Frank</i>	125
Hemagglutinin-Mediated Membrane Fusion: A Biophysical Perspective <i>Sander Boonstra, Jelle S. Blijleven, Wouter H. Roos, Patrick R. Onck, Erik van der Giessen, and Antoine M. van Oijen</i>	153
Cryo-EM Studies of Pre-mRNA Splicing: From Sample Preparation to Model Visualization <i>Max E. Wilkinson, Pei-Chun Lin, Clemens Plaschka, and Kiyoshi Nagai</i>	175
Structure and Dynamics of Membrane Proteins from Solid-State NMR <i>Venkata S. Mandala, Jonathan K. Williams, and Mei Hong</i>	201
The Molecular Origin of Enthalpy/Entropy Compensation in Biomolecular Recognition <i>Jerome M. Fox, Mengxia Zhao, Michael J. Fink, Kyungtae Kang, and George M. Whitesides</i>	223

Modeling Cell Size Regulation: From Single-Cell-Level Statistics to Molecular Mechanisms and Population-Level Effects <i>Po-Yi Ho, Jie Lin, and Ariel Amir</i>	251
Macroscopic Theory for Evolving Biological Systems Akin to Thermodynamics <i>Kunibiko Kaneko and Chikara Furusawa</i>	273
Photoreceptors Take Charge: Emerging Principles for Light Sensing <i>Tilman Kottke, Aibua Xie, Delmar S. Larsen, and Wouter D. Hoff</i>	291
High-Resolution Hydroxyl Radical Protein Footprinting: Biophysics Tool for Drug Discovery <i>Janna Kiselar and Mark R. Chance</i>	315
Dynamic Neutron Scattering by Biological Systems <i>Jeremy C. Smith, Pan Tan, Loukas Petridis, and Liang Hong</i>	335
Hydrogel-Tissue Chemistry: Principles and Applications <i>Viviana Gradinaru, Jennifer Treweek, Kristin Overton, and Karl Deisseroth</i>	355
Serial Femtosecond Crystallography of G Protein–Coupled Receptors <i>Benjamin Stauch and Vadim Cherezov</i>	377
Understanding Biological Regulation Through Synthetic Biology <i>Caleb J. Bashor and James J. Collins</i>	399
Distinct Mechanisms of Transcription Initiation by RNA Polymerases I and II <i>Christoph Engel, Simon Neyer, and Patrick Cramer</i>	425
Dynamics of Bacterial Gene Regulatory Networks <i>David L. Shis, Matthew R. Bennett, and Oleg A. Igoshin</i>	447
Molecular Mechanisms of Fast Neurotransmitter Release <i>Axel T. Brunger, Ucheor B. Choi, Ying Lai, Jeremy Leitz, and Qiangjun Zhou</i>	469
Structure and Immune Recognition of the HIV Glycan Shield <i>Max Crispin, Andrew B. Ward, and Ian A. Wilson</i>	499
Substrate-Induced Formation of Ribosomal Decoding Center for Accurate and Rapid Genetic Code Translation <i>Michael Y. Pavlov and Måns Ehrenberg</i>	525
The Biophysics of 3D Cell Migration <i>Pei-Hsun Wu, Daniele M. Gilkes, and Denis Wirtz</i>	549
Single-Molecule View of Small RNA–Guided Target Search and Recognition <i>Viktorija Globyte, Sung Hyun Kim, and Chirlmin Joo</i>	569

Behavioral Variability and Phenotypic Diversity in Bacterial Chemotaxis <i>Adam James Waite, Nicholas W. Frankel, and Thierry Emonet</i>	595
Mechanotransduction by the Actin Cytoskeleton: Converting Mechanical Stimuli into Biochemical Signals <i>Andrew R. Harris, Pamela Freij, and Daniel A. Fletcher</i>	617
The Physical Properties of Ceramides in Membranes <i>Alicia Alonso and Félix M. Goñi</i>	633
The Physics of the Metaphase Spindle <i>David Oriola, Daniel J. Needleman, and Jan Brugués</i>	655

Indexes

Cumulative Index of Contributing Authors, Volumes 43–47	675
---	-----

Errata

An online log of corrections to *Annual Review of Biophysics* articles may be found at
<http://www.annualreviews.org/errata/biophys>